HI Global Scaling Relations in the WISE-WHISP Survey

E. Naluminsa,[1]* E. C. Elson,[2] T. H. Jarrett[1]

[1] *Department of Astronomy, University of Cape Town, Private Bag X3, Rondebosch 7701, South Africa*
[2] *Department of Physics & Astronomy, University of the Western Cape, Robert Sobukwe Rd, Bellville 7535, South Africa*

ABSTRACT

We present the global scaling relations between the neutral atomic hydrogen gas, the stellar disk and the star forming disk in a sample of 228 nearby galaxies that are both spatially and spectrally resolved in HI line emission. We have used HI data from the Westerbork survey of HI in Irregular and Spiral galaxies (WHISP) and Mid Infrared (3.4 μm, 11.6 μm) data from the Wide-field Infrared Survey Explorer (WISE) survey, combining two datasets that are well-suited to such a study in terms of uniformity, resolution and sensitivity. We utilize a novel method of deriving scaling relations for quantities enclosed within the stellar disk rather than integrating over the HI disk and find the global scaling relations to be tighter when defined for enclosed quantities. We also present new HI intensity maps for the WHISP survey derived using a robust noise rejection technique along with corresponding velocity fields.

Key words: galaxies: ISM – galaxies: evolution – galaxies: star formation – galaxies: dwarf – galaxies: spiral

1 INTRODUCTION

The fundamental goal of astrophysical studies is a better understanding of the origins and evolution of our universe. Both theoretical and observational works are geared towards constructing a solid picture of the processes involved in the formation of cosmic structures. This involves pursuing accurate models of galaxy formation and evolution. Central to the evolution of galaxies is the process of star formation (SF) which must be properly accounted for in models of both chemical and physical evolution (e.g. Boissier & Prantzos 1999; Lia et al. 2002; Davé et al. 2017). This is because SF drives the consumption of gas in galaxies and the chemical and physical evolution of both the interstellar medium (ISM) and intergalactic medium (IGM) (de Blok et al. 2015).

The scaling of SF (measured in terms of star formation rate, SFR, and star formation efficiency, SFE) with other galaxy properties such as mass and mass surface density provides insights into how gas is utilized at difference epochs via collapse, accretion, ejection and recycling. A fundamental scaling relation is the Kennicutt-Schmidt (KS) law (Schmidt 1959; Kennicutt 1989, 1998) which relates the surface densities of SF and gas (atomic or molecular hydrogen) by a power law;

$$\Sigma_{\mathrm{SFR}} \; = \; A\Sigma_{\mathrm{g}}^{\mathrm{N}}, \tag{1}$$

where Σ_{SFR} is the star formation rate surface density (in $\mathrm{M}_\odot$ kpc^{-2} yr^{-1}), Σ_{g} is the gas surface density (in $\mathrm{M}_\odot$ pc^{-2}) and A is a constant of proportionality. Kennicutt (1998)

found index N = 1.4$\pm$0.05 using a combination of Σ_{HI} and $\Sigma_{\mathrm{H_2}}$ for total gas surface density. However, over the years, different studies have found varying values of N. Most notably, it has been shown that the value of N is closer to 1.0 when the surface density of molecular hydrogen gas (as traced by CO) is used instead of the total gas surface density, especially in molecule-rich ISM conditions such as the central regions of star forming spiral galaxies (e.g. Wong & Blitz 2002; Bigiel et al. 2008; Leroy et al. 2013; Dessauges-Zavadsky et al. 2014). Studies such as Boissier et al. (2003); Bigiel et al. (2008); Schruba et al. (2011); Calzetti et al. (2018) have also shown that there is, at best, a nonlinear power law relationship between $\Sigma_{\mathrm{HI+H_2}}$ and Σ_{SFR} with a higher index N $\approx$ 2.0. This is attributed to the weak relationship between Σ_{HI} and Σ_{SFR} because stars form from collapsing clouds of molecular hydrogen. Still, the atomic gas does have a connection to the SFR and it has been shown that reduction in the amount of HI in galactic disks will suppress the SF (Rownd & Young 1999; Bekki et al. 2002; Fumagalli & Gavazzi 2008). More recently, there has also been renewed interest in the volumetric Schmidt-type SF law which considers the volume-densities of the gas and SFR (Krumholz et al. 2012; Evans et al. 2014; Bacchini et al. 2019). Indeed, Bacchini et al. (2019) found 'an unexpected and tight' correlation between the volume densities of SFR and atomic gas, highlighting the important role of the HI gas, especially in low-density and low-metallicity environments.

This study, a prelude to a second paper on star formation thresholds in nearby galaxies on sub-kpc scales (Paper 2 hereafter), is aimed at characterizing a sample of 228 resolved galaxies in terms of their scaling relations. The relations range from global properties of the gas disk such as the HI size-mass relation (Broeils & Rhee 1997; Wang et al. 2016) to correla-

* E-mail: elizabeth.naluminsa@uct.ac.za (EN)

tions between the gas disk, the assembled stellar disk and the star formation rate, e.g. the HI mass-stellar luminosity correlation and star forming main sequence. Such scaling relations provide us with insights into the connections between the instantaneous star formation and the gas reservoir, enable us to study the efficiency of gas consumption during star formation at various cosmic epochs, as well as to investigate mechanisms for gas replenishment such as gas accretion (e.g. Kereš et al. 2005; Oosterloo et al. 2007; Sancisi et al. 2008).

This paper is organized as follows: Section 2 presents the sample and data used, while in Section 3 we discuss the methods used to estimate the galaxy properties of gas mass, stellar mass and star formation rates. In the same section, we also present new HI intensity maps and velocity fields for 228 galaxies from the WHISP survey (Westerbork survey of HI in Irregular and SPiral galaxies, Kamphuis et al. 1996; van der Hulst et al. 2001) as well as the methodology used to derive them. In Section 4, we present and discuss the derived global scaling relations. While 4.1 and 4.2 focus on the global HI properties and the distributions of gas mass and mass-to-light ratio as functions of the 3.4 μm stellar luminosity and surface brightness, 4.3 and 4.4 focus on a sub-sample of 180 galaxies that are detected in W3 (11.6 μm, which is sensitive to the heating of the interstellar medium by star formation) to study the galaxy SF main sequence relation and the Kennicutt-Schmidt relation. We summarize our findings in Section 5.

2 SAMPLE AND DATA

The sample used in this study was chosen from the WHISP 30″ resolution data which have higher sensitivity to low HI column density structures than the full resolution (14" x 14" /sinδ) data. Also, given the distance range 5 Mpc - 30 Mpc, where 70% of the sample falls (see Figure 1), the angular resolution of 30″ enables us to investigate physical scales of ∼1 kpc. (see e.g. Sheth et al. 2002; Bigiel et al. 2008; Onodera et al. 2010; Liu et al. 2011; Kim et al. 2013; Elson et al. 2019 for studies of the star formation relation at sub-kpc scales).

Infrared data for the sample were obtained from the WISE Extended Source Catalogue (Jarrett et al. 2019) which constructed native resolution mosaics and carried out source characterization designed for large galaxies. WISE mid-IR imaging is sensitive to stellar mass (in the short-wavelength bands) and ISM activity (long wavelength bands). Galaxies in close interactions (close enough for the interaction to be seen in the infrared images) or mergers as well as poor data and non-detections were excluded. These data were visually inspected to ensure there were no disturbances on the target's IR flux by bright foreground stars. Wherever the masking or subtraction of these stars adversely compromised the disk of the galaxy, that target was dropped from the sample. Figure A1 illustrates how this was achieved. These criteria resulted in a sample of 228 galaxies. Since the resultant sample was determined by data quality, it is not biased by morphology and can be taken as a fair representation of the complete WHISP sample. The morphologies in this sample are plotted in Figure 2 against the complete WHISP sample presented by van der Hulst et al. (2001). When investigating the global star formation properties (Sections 4.3 and 4.4), only the galaxies detected in the W3 (12 μm) band were chosen, leading to
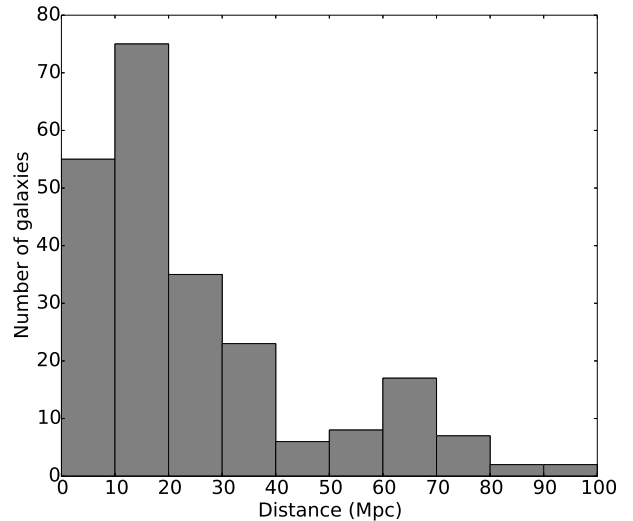

Figure 1. Distance distribution of the main sample used in this study. For these 228 galaxies, new data products have been generated (see Section 3)
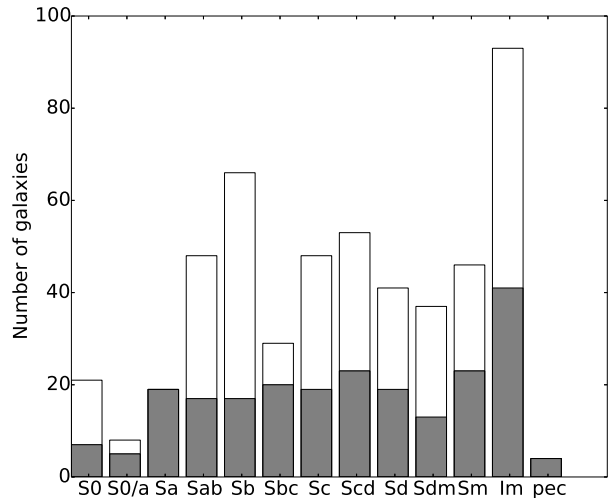

Figure 2. Distribution by morphology of the WHISP sample. The main sample used in this study (shaded area, 228 galaxies) fairly represents the entire WHISP sample (background unshaded histogram). The morphologies were obtained from the Third Reference of Bright Galaxies (RC3.9, de Vaucouleurs et al. 1991) via the NASA/IPAC Extragalactic Database (NED).

a sub-sample of 180 galaxies. Figure 3 shows images of the spiral galaxy UGC1913 in the WISE bands at 3.4 μm and 12 μm.

3 DATA PRODUCTS

The WHISP survey provides both data cubes and moment maps; however, we derived new maps by employing a strict noise-rejection technique in order to foster more robust mea-
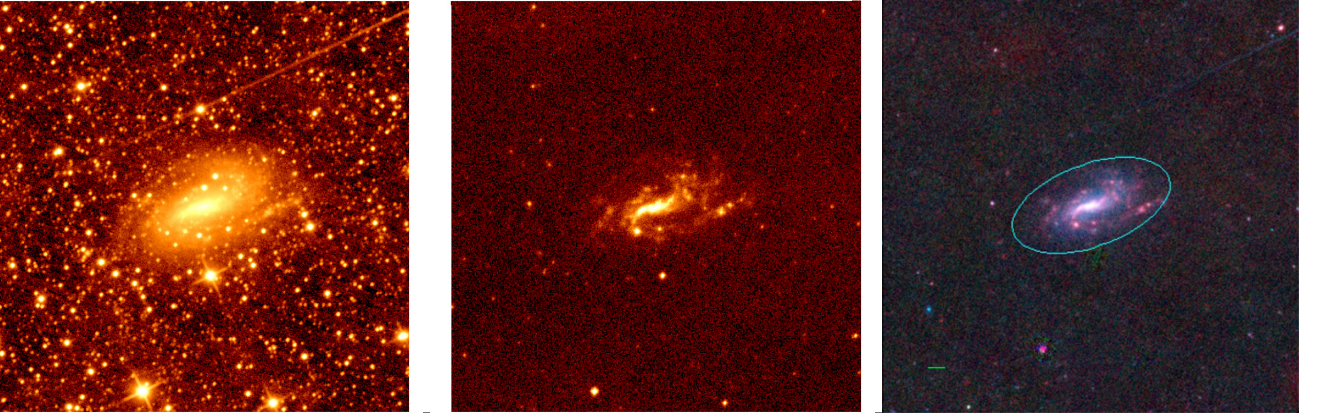
Figure 3. WISE images of UGC1913 (NGC0925) in 3.4 μm (*left*), 12 μm (*middle*) and three-color view (3.4 μm, 4.6 μm and 12 μm), with foreground stars removed, leaving only the target galaxy -*right panel*. The green scale bar shows an angular scale of 1 arcmin (2.6 kpc).

surements of the global HI properties. In this section, we describe the methods used to derive HI intensity maps and velocity fields.

3.1 HI intensity maps

$30''$ resolution data cubes were obtained from the public database of the WHISP[1] survey. The cubes were corrected for primary beam attenuation using the MIRIAD[2] *linmos* task. We describe below the process[3] we implemented to generate a new set of high-quality HI maps.

The cubes were first smoothed to $60''$. For each smoothed cube, the RMS of the flux in a line-free channel was measured. Then, all flux in the cube below the 2σ level was blanked while the flux above was marked as *True*. The resulting masks were in turn applied to the original $30''$ beam cubes to produce sigma-clipped cubes. To remove high noise peaks which survived the sigma clipping, a further step (multi-channel-peak criterion, see Noordermeer et al. 2005) was taken, where line profiles through each pixel position were inspected. Peaks detected in three or more channels were considered to be galaxy flux, but otherwise flagged as noise. Figure 4 shows examples of line profiles (from the data cube of UGC1913) showing this process. From the resulting cube, the HI intensity map was obtained by summing up the intensities from all the emission containing channels. The intensity maps from the noise clipping process before and after application of the multi-channel-peak criterion are shown in Figure 5. This same cube was used in deriving the global profiles.

In addition to the intensity distribution maps, we have derived new velocity field and dispersion maps for the WHISP sample by fitting third order Gauss-Hermite polynomials to the individual line profiles. The dispersion maps are used to model the disk gravitational instabilities in Paper II while the velocity fields will be used to derived rotation curves and study the Tully-Fisher relation in a later paper. These data
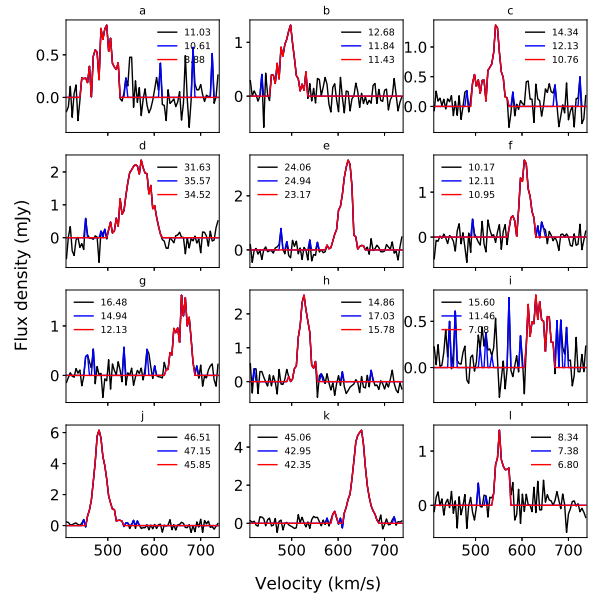
Figure 4. Line profiles at different pixel positions, drawn from the data cube of UGC1913, to illustrate the multi-channel-peak criterion. The black shows profiles from the original cube. The blue shows profiles from the sigma clipped cube which survived the 2σ clipping. These were removed by using the multi-channel-peak criterion whose resulting profiles are shown in red. The total flux under each profile is indicated by the corresponding legend. The pixel positions of the line profiles are indicated in Figure 5.

products (HI intensity maps and velocity fields and dispersion maps) will be made available upon request.

3.2 HI mass

The total HI mass was calculated from the total HI flux as,

$$\mathrm{M_{HI}(M_\odot)} \; = \; 2.36 \times 10^5 \times \mathrm{D}^2(\mathrm{Mpc}) \times \int \mathrm{S}_\nu \; \mathrm{dv} \; (\mathrm{Jy \; km \; s^{-1}}), \tag{2}$$

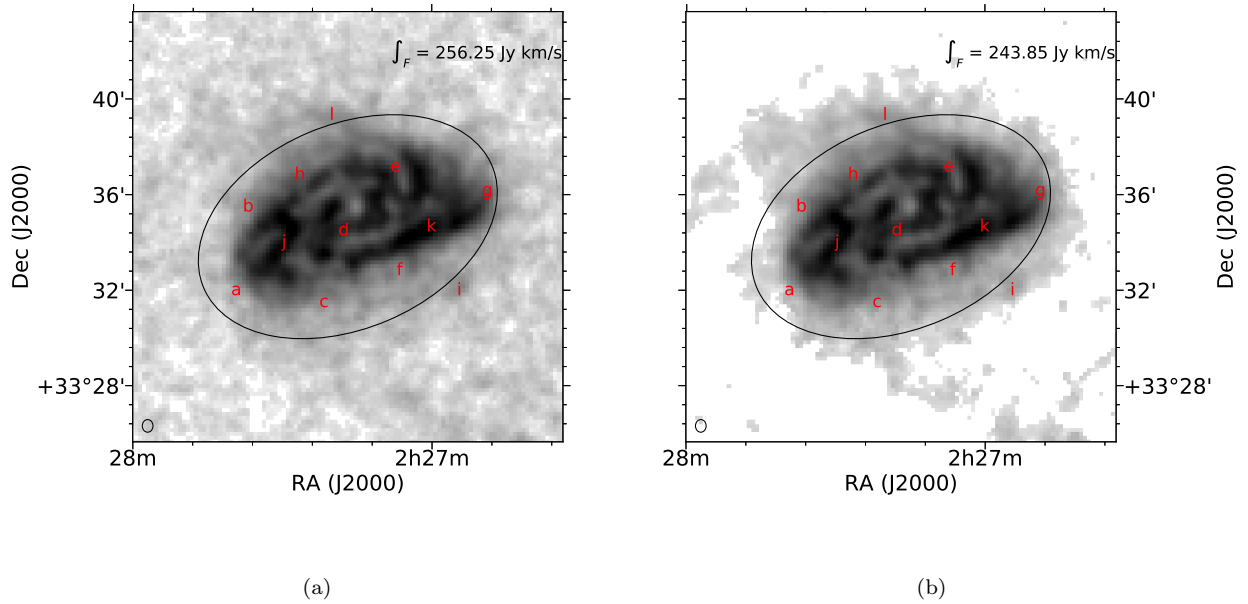(a)   (b)

Figure 5. HI intensity maps of the late-type spiral galaxy UGC1913. Panel (a) shows the result of adding up the emission in the sigma clipped cube, while (b) shows the result when the same cube is further processed using the multi-channel-peak criterion described in text. The extra step gets rid of sharp noise peaks which may be spatially coincident with the galaxy but separated in velocity space. The flux in the region enclosed by the black ellipse is shown in the upper right corner of each image. Letter labels indicate positions of the line profiles in Figure 4. The beam size ($\sim 30'' \times \sim 30''$) is shown in the lower left corner of each panel. These data products will be made available upon request.

(Brinks 2006) where D is the distance, and $\int S_\nu \, dv$ is the total HI flux integrated over the global profile. Figure 6 shows comparisons of the masses derived in this study with masses derived by two other studies that used WHISP data. These are Swaters (1999)(hereafter S99) and Noordermeer et al. (2005)(hereafter N05), with whom we had 60 and 52 galaxies in common, respectively. The masses were compared after synchronizing the distances across the samples (see Table E2 for adopted distances). The masses in this study are systematically lower than those of S99 by 0.12 dex on average. This is expected because S99 did not carry out the extra noise handling by the multi-channel-peak criterion hence having higher fluxes. On the other hand, N05 employed the multi-channel-peak criterion when generating their data products which explains why their mass estimates are in general agreement with ours. The derived total flux and mass as well as linewidths and systemic velocities for all galaxies in the sample are listed in Table E2.

3.3 HI surface density

Maps of HI surface density were obtained from the integrated flux maps as below, following the methods of Brinks (2006); Leroy et al. (2008). The HI maps were converted into column densities using the equation;

$$N_{HI} \, (cm^{-2}) \ = \ 1.823 \times 10^{18} \times \frac{\sum_\nu S_\nu}{1.65 \times 10^{-3} \times \Delta\alpha\Delta\delta} \times \Delta V, \tag{3}$$

where N_{HI} is the column density map in atoms cm^{-2}, $\Delta\alpha$ and $\Delta\delta$ are the major and minor axes of the synthesized

(a)   (b)
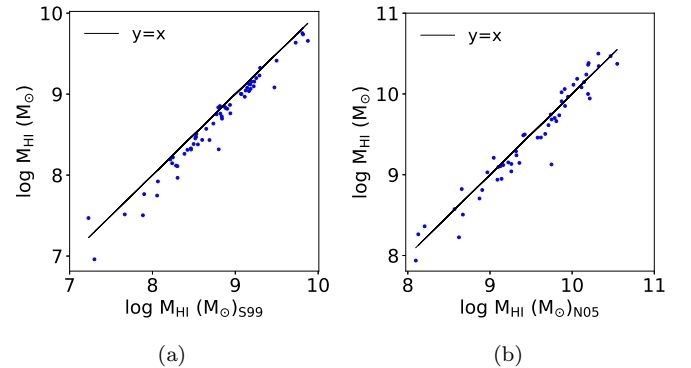
Figure 6. Comparison of mass estimates from the literature (x-axes) with this study (y-axis). S99 (a) retrieved higher fluxes from the WHISP cubes because they did not carry out the multi-peak criterion for noise removal, which N05 (b) carried out and had fluxes in agreement with ours. Note that N05 had a sample of 68 early-type spirals while S99 had sample of 73 late-type dwarfs. Our sample of 229 had 52 and 60 galaxies in common with N05 and S99. All the mass estimates shown on these plots are total integrated HI masses.

beam, ΔV is the velocity resolution in km s^{-1}, and $\sum_\nu S_\nu$ is the integrated HI map in mJy/beam. The factor in the denominator converts the intensity map into a brightness temperature map.

The column density maps were converted into surface density

maps using the equation;

$$\Sigma_{\mathrm{HI}}(\mathrm{M}_\odot \ \mathrm{pc}^{-2}) \ = \ \frac{\mathrm{N_{HI}}}{1.248 \times 10^{20}} \ \cos i, \qquad (4)$$

which accounts for inclination. Radial profiles were obtained from the inclination corrected surface density maps using the MIRIAD task *ellint* and used to derive the HI diameters at $\Sigma_{\mathrm{HI}} = 1 \ \mathrm{M}_\odot \ \mathrm{pc}^{-2}$. The threshold value of $1 \ \mathrm{M}_\odot \ \mathrm{pc}^{-2}$ was chosen in keeping with the literature (see, for example, Broeils & Rhee 1997; Verheijen & Sancisi 2001; Noordermeer et al. 2005; Wang et al. 2016)

3.4 W1 stellar mass estimation

The WISE 3.4μm (W1) band is a reliable measure for the stellar mass of galaxies because it traces the evolved stellar population which comprises the bulk of the baryonic mass in galaxies (Jarrett et al. 2013; Meidt et al. 2014). Furthermore, the near infrared does not suffer as much extinction as optical bands. We calculated stellar masses for stellar disks from the W1 absolute magnitude. The stellar disks were defined as the region enclosed by the 1σ isophote [4] in the WISE W1 images. The stellar mass empirical relations of Cluver et al. (2014) were used;

$$\mathrm{L}(\mathrm{L}_\odot) \ = \ 10^{-0.4(M \ - \ M_{sun})}, \qquad (5)$$

$$\mathrm{M}_\star(\mathrm{M}_\odot) \ = \ \Upsilon_\star^{[3.4]} \ \times \ \mathrm{L}, \qquad (6)$$

$$\log \ \Upsilon_\star^{[3.4]} \ = \ -0.17 \ - \ 2.54(\mathrm{W1} - \mathrm{W2}) \qquad (7)$$

where L is the W1 in-band luminosity, M is the absolute magnitude in the W1 band, $M_{sun} = 3.24$ is the absolute magnitude of the sun in the W1 band (Oh et al. 2008; Jarrett et al. 2013) and $\Upsilon_\star^{[3.4]}$ is the mass to light ratio. Limits were placed on the W1-W2 color ($-0.05 \leq$ W1 $-$ W2 ≤ 0.2mag) to minimize contamination by AGN light in W2 and unphysical blue colors (due to the lower sensitivity of the W2 band). Below the lower limit, the M/L was set to 0.21, and to 0.91 above the upper limit (Cluver et al. 2014; Jarrett et al. 2019). Any dwarf galaxies which were not detected in W2 or had W1-W2 colors with S/N $\leq$ 3 were assigned a constant M/L of 0.6 (Kettlety et al. 2018). The derived stellar masses for our sample are presented in Table E4. Note that the W1 band is sensitive to light from warm dust, PAH molecules (3.3 μm) and AGB stars, all of which can exaggerate the W1 flux (Meidt et al. 2012; Querejeta et al. 2015; Ponomareva et al. 2018). The independent component analysis correction for non-stellar contamination (Meidt et al. 2012) was not carried out, and hence the stellar masses quoted here should be taken as upper boundaries.

3.5 W3 SFR estimation

Measurements of Star formation were obtained from WISE W3 (11.6 μm) imaging. The W3 band is wide and spans PAH emission features at 7.7 μm, 8.5 μm and 11.3 μm, Neon nebular emission lines [Ne II] at 12.8 μm and [Ne III] at 15.6 μm, silicate absorption at 10 μm, as well as warm dust continuum (Cluver et al. 2017). The 11.6 μm band was chosen to derived SFR over the W4 (22.8 μm) band because of its superior sensitivity (Jarrett et al. 2013). Furthermore, Elson et al. (2019) have showed for M33 that the W3 band is a good monochromatic tracer of the total SFR (as typically traced by FUV + 24 um).

SFR's were derived from the spectral luminosity, $\nu \mathrm{L}_\nu$, following the empirical relations of Cluver et al. (2017) who calibrated the WISE mid-IR to the total infrared luminosity;

$$\log(\mathrm{SFR}) \ = \ (-7.76 \pm 0.15) \ + \ (0.889 \pm 0.018) \log(\nu \mathrm{L}_\nu),$$

---

[4] $\sim$23 mag arcsec^{-2} in Vega units

$$(8)$$

with

$$\nu L_\nu(L_\odot) \; = \; \frac{\nu_{w3} \; \times \; 4\pi D^2 \; \times \; f_\nu}{3.846 \; \times \; 10^{26}}, \tag{9}$$

where ν_{w3} is the mid-band frequency of the W3 band, f_ν is the W3 flux, νL_ν is the spectral luminosity in $L_\odot$ and D is the distance in meters. With these prescriptions and WISE measurements, the uncertainty in the SFRs will be about 30% (Cluver et al. 2017; Jarrett et al. 2019).

The adopted distances are listed in Table E2 while the WISE photometry and derived SFR's are presented in Tables E3 and E4.

4 SCALING RELATIONS

4.1 *The* HI *mass-size relation*

The HI masses of galaxies and their diameters defined at an HI surface density (Σ_{HI}) of 1 $M_\odot$ pc^{-2} are known to be tightly correlated. This relation has been observed to hold across three and five orders of magnitude in diameter and mass respectively (Wang et al. 2016), for morphologies ranging from early-type spirals to dwarfs and irregulars (Broeils & Rhee 1997; Verheijen & Sancisi 2001; Swaters et al. 2002; Noordermeer et al. 2005; Martinsson 2011; Wang et al. 2014; Ponomareva et al. 2016). The relations found by the different authors have slopes of 1.84±0.12 in log space. Swaters et al. (2002) and Noordermeer et al. (2005) derived this relation for 73 dwarf irregulars and 68 early-type spirals respectively in the WHISP sample. Here we present this relation for 228 WHISP galaxies, spanning from early-type spirals to dwarf irregulars and find the relation to be in agreement with previous studies within the errors. We find the tight relation below:

$$\log M_{HI} \; = \; (1.95 \pm 0.03) \log D_{HI} \; + \; (6.5 \pm 0.04), \tag{10}$$

which has a dex error of 3% on the slope, 4% on the intercept and a vertical scatter of 0.14 about the best-fit line. The relation for our sample is in particularly good agreement with the relations of Broeils & Rhee (1997) and Wang et al. (2016) who had slopes of 1.96±0.04 and 1.98±0.01 respectively, and whose samples were complete comprising of all morphological types from early-type spirals to dwarfs as did our sample. Our slope is steeper than other studies by Verheijen & Sancisi (2001); Swaters et al. (2002); Noordermeer et al. (2005); Ponomareva et al. (2016) mostly because their samples were less complete, consisting only of either spirals or dwarfs. Note that the Wang et al. (2016) study included 100 WHISP galaxies in their sample of 549.

Such a power law relates the approximate square of the diameter against the mass, giving a typical mean HI surface density across galaxy disks (Broeils & Rhee 1997). That this relation is found consistent for samples across all morphologies and in different environments implies that *the* HI *disks regulate themselves to a typical mean value of surface density* (Verheijen & Sancisi 2001; Noordermeer et al. 2005). Having used analytical models and cosmological simulations for galaxies at z=0, Stevens et al. (2019) attribute this property of galaxies to the general distribution of HI in disks and
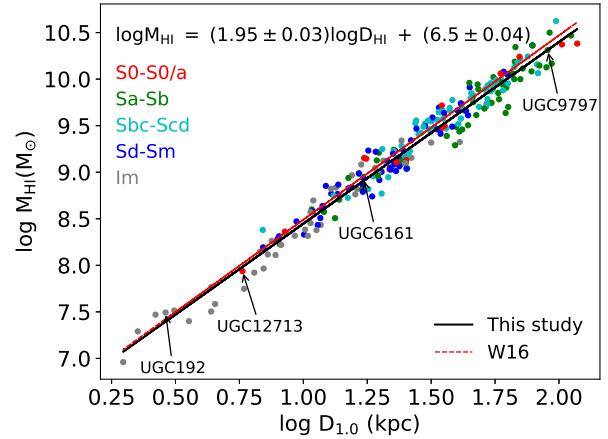
Figure 7. HI mass versus HI diameter for all galaxies in our sample. The data points are color coded by the morphology of the galaxies such that the red represents lenticulars (S0-S0/a), green represents early type spirals (Sa-Sb), cyan represents Sbc - Scd, blue represents late-type spirals (Sd-Sm) and the gray are the late-type dwarfs. A fit to the data is shown by the black solid line. The relation of Wang et al. (2016) (W16) is shown as a red dashed line. The Broeils & Rhee (1997), Verheijen & Sancisi (2001) relations are very similar to the W16 relation. The HI diameters were defined at the 1 $M_\odot$ pc^{-2} level of the radial profiles while HI masses were determined from the total flux in the global profiles. The mass-size relation of HI disks is an indicator of a constant average HI surface density. Note: One galaxy, UGC3826, had Σ_{HI} $\leq$ 1 $M_\odot$ pc^{-2} across it's entire disk, and hence was not used when deriving the mass-size relation.

its tendency to saturate due to the HI - H_2 phase transition, showing that even quenching and disk truncation will only change the relative position of a galaxy on the relation but will not completely remove it. Figure 7 is a plot of our data, overlaid with the relations of Broeils & Rhee (1997), Verheijen & Sancisi (2001) and Wang et al. (2016). Late-type dwarfs such as UGC192 (IC10) populate the low mass end of the relation while early-type spirals such as UGC9797 (NGC5905) are found at the high mass end. Exceptions exist such as an early-type at the low mass end which is the case for UGC12713, a dwarf spheroidal. However, this is in keeping with the correlation that the smaller HI disks contain lower HI masses regardless of morphological type.

4.2 HI *mass vs stellar luminosity*

The relationships between the HI mass and stellar disk properties of luminosity and surface brightness represent the scaling relations between the ISM which is a reservoir of fuel for star formation and the galaxy's underlying baryonic mass in the form of the old stellar population. The HI mass derived here is the mass enclosed within the stellar disk, defined by a 1σ isophote in the W1 image at surface brightness $\sim$ 23 mag arcsec^{-2} (Vega units), which incorporates more than 95% of the total flux (Jarrett et al. 2019). This gives us a direct comparison between the atomic gas reservoir for star formation spatially co-located with the stellar disk.

Figure 8 illustrates the relationships between the HI mass contained within the stellar disk, and stellar disk magnitude and surface brightness. The plots are also color-coded accord-
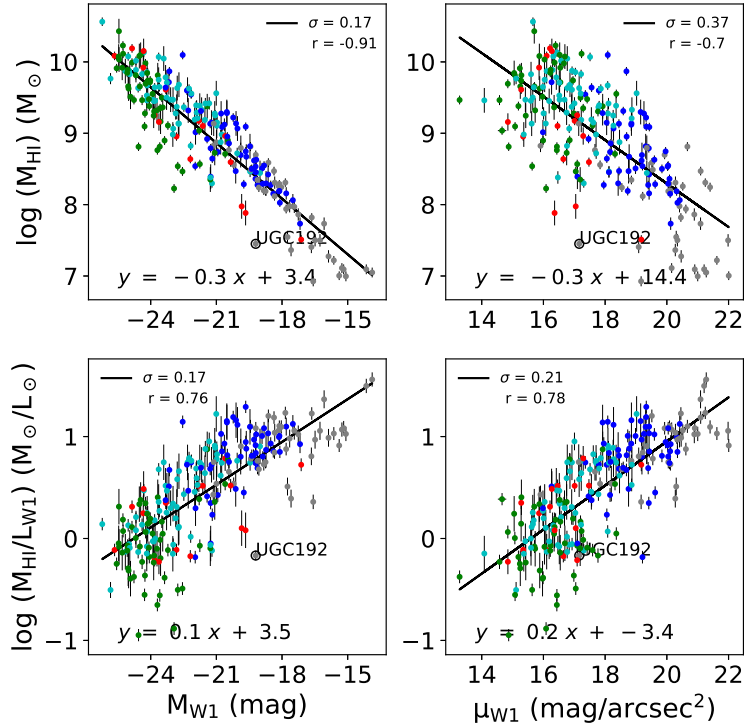
Figure 8. Plots of HI mass (upper panels) and HI mass-to-light ratio (lower panels) versus 3.4 μm absolute magnitude which is a direct measure of the stellar mass (left panels) and mean surface brightness over the stellar disk (right panels). Note that these are 'enclosed quantities' measured within the stellar disks. The correlation coefficient (r) for each plot and the vertical scatter (σ) about the fitted line are shown in the upper left/right corners of the plots. For most points, the errors on the x axes are smaller than the data points. The plots are also color-coded according to morphological type such that red represents lenticulars (S0-S0/a), green represents early type spirals (Sa-Sb), cyan represents Sbc - Scd, blue represents late-type spirals (Sd-Sm) and the gray are the late-type dwarfs.

ing to morphological type such that red represents lenticulars (S0-S0/a), green represents early type spirals (Sa-Sb), cyan represents Sbc - Scd, blue represents late-type spirals (Sd-Sm) and the gray are the late-type dwarfs. The 'r' labels in the plots are the correlation coefficients while 'σ' denotes the vertical scatter about the least squares fits to the data (solid line). All the plots show strong correlation coefficients between the properties. This is in agreement with the complete (although smaller) sample of Verheijen & Sancisi (2001), as well as the sample of Ponomareva et al. (2016), although the Ponomareva et al. (2016) study found a weaker correlation (0.64) between the M_{HI} and stellar luminosity.

From a morphological point of view, the late-type dwarfs have lower luminosities (intrinsically fainter) and higher surface brightness than the earlier type spirals. The intrinsic brightness decreases across the Hubble sequence from early-type spirals to late-type dwarfs. We also see that the enclosed HI mass decreases from early-types towards late-types while on the other hand the gas-star fraction increases towards the late-types.

Note that our relations derived for the atomic gas enclosed within the stellar disk follow the same trend as those from previous studies that used integrated properties over the entire HI disk. However, there is clearly less scatter in our relation between M_{HI} and M_{W1}, as would be expected, because

we are comparing spatially co-located properties in the stellar disk.

UGC192 (IC10, a blue compact dwarf) is an outlier in all four plots. In the bottom panels, it shows much lower gas fraction (M_{HI}/M_*) than the rest of the dwarfs and is tending toward the spiral regime in luminosity and surface brightness. This is because (i) the quantities presented here are calculated within the W1 stellar disk, while UGC192 has been shown to have a significant amount of its HI gas in an extended stream beyond the main disk (Wilcots & Miller 1998) and (ii) this galaxy is a starburst dwarf irregular galaxy exhibiting high star formation rates like the spirals and producing more energy than a regular dwarf, hence its high infrared luminosity (Figure 9 shows a WISE three-color illustration of UGC192). On the other hand we have UGC12713 a dwarf spheroidal in a zone populated by late-type dwarfs. This shows that the apparent scaling of these quantities with morphology is not a cause but rather an effect of the underlying scaling relations amongst the quantities themselves and processes such as star formation. We find that galaxies with higher gas factions are intrinsically fainter in W1, i.e. they have lower stellar luminosity, than those with low gas fractions. Roberts (1969) suggested that the gas fraction may decrease towards earlier type spirals, which indeed shows in the lower panels of Figure 8 where the early-type spirals,

populate the low gas fraction part of the plots. The mass luminosity scaling relations in our sample are in agreement with those of Verheijen & Sancisi (2001) taken from the Ursa major galaxy cluster.

The M_{HI} - M_* relation for our WHISP sample is plotted in Figure 10. In general, there is a relatively tight correlation whereby the M_{HI} increases with the M_*, but the relation might be non-linear at the high-mass end. A maximum likelihood fit to the data yields a slope of 0.71 ± 0.02 (solid black line). At log $M_* \sim 9$, we observe the high mass Sa-Sb and S0 galaxies shifting below the relation, perhaps the beginning of an apparent migration off the relation by gas deficient early types. A flattening which depicts a lower dependence of the gas mass on the stellar mass at the high-mass end has been observed by studies such as Catinella et al. (2010); Huang et al. (2012); Maddox et al. (2015, 2016). Given that our sample includes very few S0's and no ellipticals, we, like Parkash et al. (2018) and their HICAT-WISE study, are unable to see the actual flattening of the relation which occurs for the early types with low gas fractions (see Catinella et al. 2010). The salient difference in slopes between our study and Parkash et al. (2018) is because we use the HI mass enclosed within the stellar disk. For comparison, a fit using the total M_{HI} (from the global profile) for our WHISP sample is shown with the solid magenta line in Figure 10, and lies closer to the Parkash slope. The main factor is that the HI disks of the gas rich spirals and dwarfs tend to be more extended than their optical disks (Swaters et al. 2002; Wang et al. 2013; Koribalski et al. 2018; Wang et al. 2020). Given the low stellar masses of dwarfs, hence lower disk gravitational potential, the gas is less concentrated and the effect of using stellar disk enclosed M_{HI} is more pronounced in the dwarfs regime, leading to steepening of the M_{HI} - M_* slope at the low-mass end. In contrast, the fits tend to converge on the high-mass end, implying that most of the M_{HI} in the early types is contained within the stellar disks.

From the relations observed in this section we find that the global HI properties of our galaxy sample are in agreement with other samples and scale as expected, although with a different slope because of the aperture matching between the HI and the infrared. This means that our galaxy sample is a balanced representation of the general galaxy population in terms of the HI content and stellar luminosity.

4.3 *The Star formation main sequence relation*

The correlation between star formation rate and stellar mass, known as the star formation main sequence (SFMS), is a well established scaling relation in galaxies (Brinchmann et al. 2004; Noeske et al. 2007; Daddi et al. 2007; Rodighiero et al. 2010; Wuyts et al. 2011) with a remarkably tight scatter of 0.2 dex, and has been shown to hold over all redshifts up to z=6 (Speagle et al. 2014). This relation depicts the star forming histories (SFH) of galaxies in the universe since it compares the instantaneous star formation to past star formation. It defines the rate at which galaxies build their mass, with the more massive galaxies assembling their mass earlier on in cosmic history. The SFMS is therefore an important constraint on the mass assembly histories of galaxies and is widely applied in models of galaxy formation and evolution (e.g., Peng et al. 2010; Leitner 2012; Behroozi et al. 2013; Henriques et al. 2015; Sparre et al. 2015). The scatter in the relation has been observed to increase at the high mass end, a feature attributed to the widely varying SFHs among massive galaxies including minor and satellite merger events.

Figure 11 illustrates our main sequence relation for a sub-sample of 180 galaxies which are detected in the W3 band. The data are color coded by the W2-W3 color where blue, cyan, orange and red represent W2-W3 ≤ 2, ≤ 3.0, ≤ 3.5 and, ≥ 3.5 respectively. The W2-W3 is an indicator of the dust content but also roughly follows the morphologies such that low star forming early-types have bluer colors in the mid-IR bands while the high star forming intermediate spirals have redder colors (following the color-code convention of Cluver et al. 2017). Our sample galaxies follow a well defined main sequence with a scatter of 0.4 dex. In agreement with previous studies (e.g Guo et al. 2015; Ilbert et al. 2015; Jarrett et al. 2017; Cluver et al. 2017), there is an increase in scatter at the high mass end partly due to the prevalence of gas exhaustion in high mass systems Noeske et al. (2007). Passive evolution as well as processes such as mergers, quenching or gas stripping lead to declining SFRs, eventually causing the affected galaxy to migrate from the main sequence or its current SFR being decoupled from its past SFR (Ilbert et al. 2015; Jarrett et al. 2017; Cluver et al. 2020).

Having decomposed their sample galaxies into disks and bulges, Guo et al. (2015) suggest that the increased variations in the SFHs of massive galaxies are due to the prevalence of central dense structures such as bars and bulges in massive systems. A bulge that is not star forming contributes to the total stellar mass of a galaxy but not to the total star formation, yielding a specific star formation rate ($sSFR = SFR/M_*$) lower than that for a disk dominated system. The varying masses of the bulges affect the derived sSFR to different extents hence we see scatter in the relation, leaving the disk dominated systems to have more similar SFHs and hence a tighter main sequence relation. This may well be the reason for the clear segregation seen between the different morphological types in Figure 11, suggesting different SF main sequences for the different galaxy types. Cluver et al. (2020) have demonstrated the sensitivity of the SFMS relation to sample selection criteria such that star forming samples yield steeper relations than samples which include galaxies that have turned over at the high mass end. Indeed their sample which excludes the low mass - low SFR population ($M_* < 10^{9.75}$, $W2 - W3 \leq 3$) has a shallower SFMS
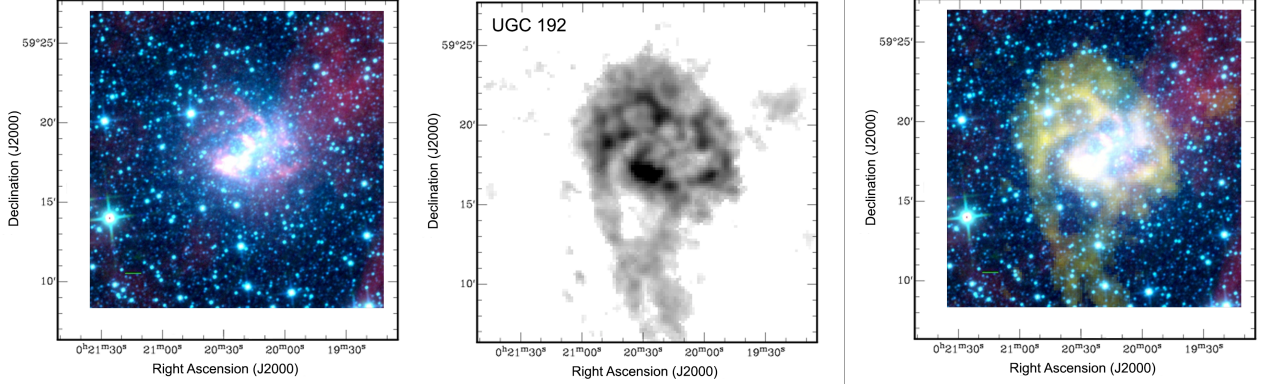
Figure 9. Star Formation and Gas Reservoir of UGC192. *Left*: A WISE three-color image of UGC192, with 3.4 μm (blue), 4.6 μm (cyan/green) and 11.6 μm (red). *Middle*: HI intensity distribution showing the disturbed morphology of UGC192 with a southern plume that has been suggested to be due to accretion of low column density primordial material (see Wilcots & Miller 1998; Namumba et al. 2019). Notice the spatial coincidence of the higher density HI clumps with the bright SF regions in the 11.6 μm emission. UGC192 is a star-bursting dwarf galaxy (a blue compact dwarf, BCD) in the local group. It has stellar mass $10^{8.6}$M$_\odot$ much higher than its gas mass ($10^{7.4}$M$_\odot$) and thus has a low gas fraction (0.06) that is similar to star forming spirals which place lower on the y-axis in the lower panels of Figure 8. Its absolute magnitude (stellar luminosity) is not atypical of the dwarfs in the sample (see left panels of Fig 8), but its surface brightness is exceptionally high (due to the starburst) and places it in the spiral-populated region in right panels of Figure 8. (see also Figure 13). *Right panel*: Combined HI and three-color WISE image showing the extent of the obscured star formation with respect to the HI disk. The green scale bar in the lower left corner shows an angular scale of 1 arcmin (0.2 kpc).
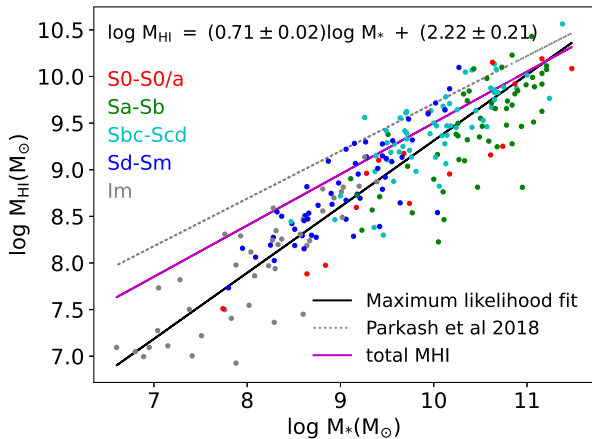

Figure 10. Enclosed HI mass versus stellar mass. The data points are color coded by the morphology of the galaxies such that the red represents lenticulars (S0-S0/a), green represents early type spirals (Sa-Sb), cyan represents Sbc - Scd, blue represents late-type spirals (Sd-Sm) and the gray are the late-type dwarfs. The solid black line indicates our best fit function to the data, with parameters shown in the upper left. Note that the M$_{\rm HI}$ used here is the HI mass contained within the stellar disk (see Section 3.4). For comparison, a fit to the total M$_{\rm HI}$ (from the global profile) for our WHISP sample is shown in magenta and lies closer to the Parkash et al. (2018) HICAT sample fit (gray line) which also used total M$_{\rm HI}$.

(slope = 0.93) than our sample which includes M$_* < 10^9$ and W2 $-$ W3 $\leq$ 2. Likewise, we compare our relation to the SFMS relation of Parkash et al. (2018). Their SFMS was modeled using high stellar-mass (M$_* \geq 10^{10.5}$ M$_\odot$) spirals, close to the turnover at high-mass, resulting in an even shallower slope of 0.7.

In Figure 12, we plot the sSFR against stellar mass and find

a mostly flat trend which turns downward, tending to a negative slope, for the high mass galaxies. This trend, which was also found by Jarrett et al. (2017) and Cluver et al. (2020), shows that even though the low mass galaxies have lower SFRs than the high mass systems, the former are still in an active stage of building their disks while the latter are progressing toward passive or quiescent star forming states (Jarrett et al. 2017). For example UGC7256 (NGC4203) is a lenticular galaxy with ongoing SFR but given its stellar disk of $\sim 10^{10.6}$ M$_\odot$ (and stellar mass to light ratio = 0.73), it has a low sSFR and is no longer actively building its disk. This is also the case for UGC3993 and UGC2487 (NGC1167). These three also have low gas fractions (≤ 0.04). On the other hand UGC3334 (NGC1961) has a considerable bulge to total disk ratio (0.71), has one of the highest stellar masses in the sample ($\sim 10^{11.4}$ M$_\odot$), but is also dusty (W2-W3 = 3.25) with a higher gas fraction (0.15) and sSFR ($\sim 10^{-10.1}$ yr^{-1}). Note that in high mass systems there can be cases of enhanced star formation even after the galaxy has assembled its mass, for example in the case of merger events. Such events will cause the affected galaxy to migrate upwards and as the enhanced SF period phases out it will migrate again down towards passive SF. We find, as did Cluver et al. (2020), that it is the more dusty systems (large W2-W3 colors) which have the highest sSFR. For example, UGC5786 (NGC3310) and UGC 6001 (NGC3442) have the highest sSFR and highest dust content, (W2 $-$ W3 $\geq$ 4).

We have over-plotted the sSFR-M$_*$ relation of Grootes et al. (2013) in Figure 12. Their sample-selection was based on NUV detection which is more more sensitive to relatively dust-free SF systems, notably dwarf systems, and hence the high sSFR for the low mass end (see Jarrett et al. 2017).

Note that there are few late-type dwarfs in our SFMS subsample because most of them have very low dust contents and lie below the W3 detection threshold. The W1 band is very sensitive and well able to detect these dwarfs and their
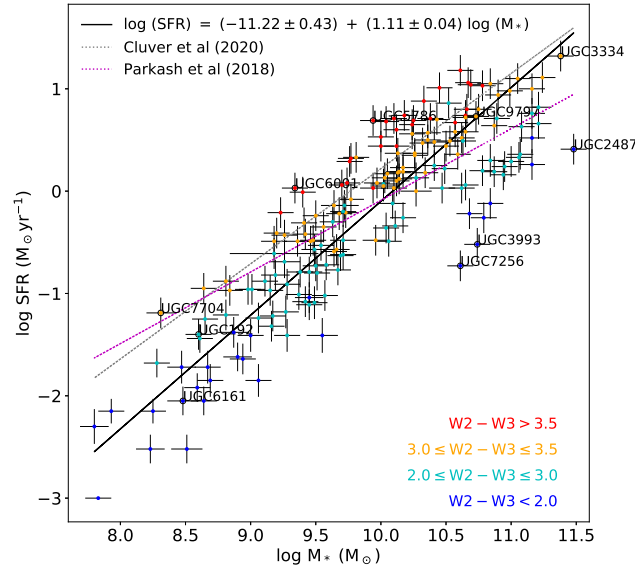
Figure 11. Relation between SFR and stellar mass for 180 galaxies detected in W3. The plot is color coded by the W2-W3 color where blue, cyan, orange and red represent W2-W3 ≤ 2, ≤ 3.0, ≤ 3.5 and, ≥ 3.5 respectively. The W2-W3 is an indicator of the dust content but also follows the morphologies such that low star forming early-types have bluer colors while the high star forming intermediate spirals have redder colors (we have followed the color-code convention of Cluver et al. 2017). The solid black line is a maximum likelihood fit to the data. For a given mass range, the main sequence line marks a separation between early-types and late-types.
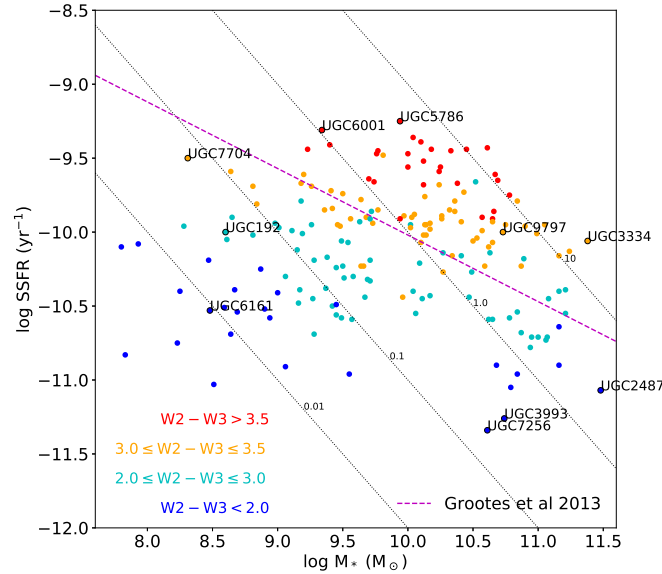
Figure 12. Relation between the specific SFR ($sSFR = SFR/M_*$) and stellar mass. The plot is color coded by the W2-W3 color where blue, cyan, orange and red represent W2-W3 ≤ 2, ≤ 3.0, ≤ 3.5 and, ≥ 3.5 respectively. The black dashed diagonal lines represent lines of constant SFR (0.01, 0.1, 1, and 10 $M_\odot yr^{-1}$). The dashed magenta line is the relation of Grootes et al. (2013) whose sample of spirals had $\log M_* \geq 9.6$.

Table 1. Specific properties of galaxies labeled in Figures 11 - 13: (1) - Name. (2) - stellar mass. (3) - Atomic hydrogen mass. (4) - Star formation rate as measured from W3 flux calibration. Note that the SFR is integrated over the stellar disk. (5) - Specific star formation rate. (6) - $W2 - W3$ color index. (7) - Gas fraction, that is, the ratio of HI mass to the stellar mass, both quantities summed up inside the stellar disk. (8) - Morphology.

Name	$\log(M_*)$	$\log(M_{HI})$	$\log(SFR)$	$\log(sSFR)$	W2-W3	$\frac{M_{HI}}{M_*}$	Morph
	$M_\odot$	$M_\odot$	$M_\odot yr^{-1}$	yr^{-1}	mag		
(1)	(2)	(3)	(4)	(5)	(6)	(7)	(8)
UGC192	8.6	7.45	-1.4	-10.0	2.75	0.07	Im
UGC2487	11.48	10.08	0.41	-11.07	1.83	0.04	S0
UGC3334	11.38	10.56	1.32	-10.06	3.39	0.15	Sc
UGC3993	10.74	9.25	-0.52	-11.26	1.35	0.03	S0
UGC5786	9.94	9.61	0.69	-9.25	4.26	0.47	pec
UGC6001	9.34	8.57	0.03	-9.31	4.03	0.17	Sa
UGC6161	8.48	8.42	-2.05	-10.53	1.8	0.88	Sdm
UGC6713	8.51	8.36	-2.52	-11.03	0.82	0.71	Sm
UGC7232	7.83	7.41	-3.0	-10.83	1.26	0.38	Im
UGC7256	10.61	9.16	-0.73	-11.34	1.15	0.04	S0
UGC7704	8.31	8.35	-1.19	-9.5	3.25	1.09	Im
UGC9797	10.73	10.1	0.73	-10.0	3.48	0.23	Sb

stellar mass, but this is not the case for W3. Also note; Table 1 lists specific properties of the galaxies labelled in Figures 7 - 13, for reference with the plots.

4.4 *Star formation rate vs* HI *mass*

The disruption of the atomic gas leads to suppression of star formation because atomic gas is needed to cool and form the molecular clouds (Fumagalli & Gavazzi 2008; Elmegreen & Hunter 2015) from which the stars form.

In Figure 13 (left panel), we plot the SFR as a function of the atomic gas mass enclosed within the stellar disk. The plot is color-coded by gas fraction ($f_g = M_{HI}/M_*$) such that red represents $f_g \leq 0.15$, cyan $0.15 \leq f_g \leq 0.6$ and blue $f_g > 0.6$. The galaxies with low gas fractions are mostly early type spirals such as UGC2487 (S0), UGC3993 (S0) and UGC6001 (Sa). Right away, it is clear that the relationship between SFR and M_{HI} holds at different f_g. There is a general trend that at any given gas mass, the galaxies with low f_g have higher SFR, a trend that remains even when the parameters are normalized by surface area (see right panel of Figure 13).

Overlaid on the data in Figure 13 (left panel) are; a least squares fit with slope 1.1 ± 0.1, a best fit line (maximum likelihood[5]) with a slope of 1.6 ± 0.1, as well as the relations of Cluver et al. (2010) for galaxies in the Spitzer Infrared Nearby Galaxies survey (SINGS[6]) and Michałowski et al. (2015). These two relations have slopes 1.1 and 1.3 respectively, in agreement within the errors, with our least squares fit which only minimizes the square residuals overall. However, the maximum likelihood fit highlights a feature in the data where the high mass end is biased by galaxies with low f_g while the low mass end is biased by galaxies with high f_g. These two groups separately appear to have different relations. To investigate this, we binned the data by gas fraction into two groups separated at $f_g = 0.15$ and applied maximum likelihood fits to each. The thin gray lines are the result showing a shallow slope (0.9 ± 0.1) for $f_g \leq 0.15$ (the red color code which are early-type spirals), and a steeper slope

(1.5±0.1) for $f_g > 0.15$ (blue and cyan, which are intermediate and late-type). The early types, even though having higher total atomic gas mass, have already assembled the bulk of their stellar mass and hence have lower gas fractions. Likewise their SFR's do not increase significantly with mass, because they are moving into a more quiescent stage of star formation (see Section 4.3), hence resulting in a shallow relation. On the other hand, the later type spirals are still actively building their disks and still have high gas fractions resulting in a steeper difference between SFR for different M_{HI}.

In the right panel of Figure 13, we plot the surface densities of SFR and M_{HI}. Note that here we refer to the integrated HI surface density, obtained from dividing the M_{HI} enclosed in the stellar disk (as defined in Section 3.4) by the de-projected area of the stellar disk. We do not trace any correlation between the two quantities, due to the limited range of HI surface densities (one magnitude) spanned by our sample. This limitation partly arises from the tight mass-size relation of spiral galaxies (see Section 4.1) whose consistent slope of ~ 2 for a wide variety of samples (Wang et al. 2016) implies a roughly constant characteristic average HI surface density for all star forming galaxies (Verheijen & Sancisi 2001; Noordermeer et al. 2005; Martinsson 2011). The SFR, on the other hand, is not regulated by disk size (or projected surface area) so the Σ_{SFR} spans a wider range of three orders of magnitude. Note that our entire sample falls on the steep part of the relation of Bigiel et al. (2008) (See their Figure 10).

A study of the resolved disks rather than global averages would give a fair comparison between the surface densities of atomic hydrogen and SFR. In Paper II, we carry out a resolved study of the gas density threshold for star formation in light of two models of disk stability, where we investigate the necessary critical density/stability parameter for the onset of star formation.

5 SUMMARY AND CONCLUSIONS

Having derived new HI intensity maps for the WHISP survey, we have measured global relations between HI and stellar disk properties using WHISP 21cm line observations and WISE 3.4 μm imaging for 228 galaxies. We have also

[5] http://hyperfit.icrar.org/, Robotham & Obreschkow (2015)
[6] http://irsa.ipac.caltech.edu/data/SPITZER/SINGS/

Figure 13. *Left panel*: Star formation rate versus atomic gas mass. The HI masses were derived from gas enclosed within the stellar disk defined by the 1σ isophote in the W1 images ($\sim$23 mag arcsec^{-2} in Vega units). The points are color-coded by gas fraction (f$_g$ = MHI/M$_*$) such that red represents f$_g \leq 0.15$, cyan for $0.15 \leq$ f$_g \leq 0.6$ and blue for f$_g > 0.6$. The color code highlights a 'green valley' and apparent red and blue sequences (fit by the two thin gray lines - discussed in the text) with a few outliers. Our maximum likelihood best fit (solid black line) is shown together with the lines of Cluver et al. (2010) and Michałowski et al. (2015). *Right panel*: Mean star formation rate surface density versus HI surface density for the sub-sample. The surface densities were averaged over the entire stellar disk defined by the 1σ isophote in the W1 images. The plot is color coded by gas fraction (f$_g$ = MHI/M$_*$) such that red represents f$_g \leq 0.15$, cyan for $0.15 \leq$ f$_g \leq 0.6$ and blue for f$_g > 0.6$. There is no correlation observed between the Σ_{HI} and Σ_{SFR} at these global scales.

studied the star forming main sequence (SFR vs M$_*$) for a sub-sample of 180 galaxies detected in the WISE 12 μm band, as well as the relationship between SFR and M$_{HI}$. We find the following:

1. Our sample of 228 galaxies fall on the HI mass-size relation with slope 1.95±0.03, and a characteristic mean HI surface density, both in agreement with the literature on studies of complete samples.

2. Correlations of the M$_{HI}$ and HI mass-to-light ratio (M$_{HI}$/L) with stellar luminosity and surface brightness (μ_{W1}) have lower scatter when considered for M$_{HI}$ enclosed within the stellar disk than when total integrated masses are used. We obtained vertical scatter of 0.17 for the relations with stellar luminosity while the relations for μ_{W1} have a scatter of 0.37 for M$_{HI}$ and 0.21 for M$_{HI}$/L. Thus the relations for stellar luminosity are tighter than those for stellar surface brightness.

3. The general trends in our relations are the same as in other studies which use integrated properties over the entire HI disk. The M$_{HI}$ is negatively correlated with the stellar luminosity and μ_{W1} (R=0.9 and R=0.7 respectively) while M$_{HI}$/L is positively correlated with the same (R=0.76 and R=0.78). Note that we obtain a tight relation for M$_{HI}$ vs M$_{W1}$ as a result of comparing spatially co-located quantities in the stellar disk.

4. The early-type spiral galaxies tend to have higher stellar luminosity and higher M$_{HI}$, but lower M$_{HI}$/L than late-type spirals and dwarfs.

5. Our sample follows a SF main sequence of slope 1.1 with

a vertical scatter of 0.4. There is a segregation between the galaxies with higher dust content (which typically have higher SFR at any given constant stellar mass) above the main sequence and the galaxies with lower dust content (lower SFR) below the main sequence.

6. There is a characteristic migration of the high M$_*$ galaxies off the main sequence towards lower SFR, which may be due to quenching, gas stripping or mergers the end result of which is passive evolution.

7. We find a correlation between SFR and M$_{HI}$ in agreement with the literature, albeit with a large scatter of 0.6. The SFR-M$_{HI}$ relation appears to be driven by the gas fraction and stellar mass of the galaxies.

8. We find no correlation between the global average surface densities of SFR and atomic gas because of the small range in magnitude spanned by Σ_{HI}. This is, atleast in part, due to the HI mass-size scaling relation which results in a roughly constant characteristic average surface density for HI disks.

DATA AVAILABILITY

The data products (HI distribution maps and velocity fields) generated in this research will be made available upon reasonable request to the corresponding author.

REFERENCES

Bacchini C., Fraternali F., Iorio G., Pezzulli G., 2019, A&A, 622, A64

Behroozi P. S., Wechsler R. H., Conroy C., 2013, ApJ, 770, 57

Bekki K., Couch W. J., Shioya Y., 2002, ApJ, 577, 651

Bigiel F., Leroy A., Walter F., Brinks E., de Blok W. J. G., Madore B., Thornley M. D., 2008, AJ, 136, 2846

Boissier S., Prantzos N., 1999, MNRAS, 307, 857

Boissier S., Prantzos N., Boselli A., Gavazzi G., 2003, MNRAS, 346, 1215

Brinchmann J., Charlot S., White S. D. M., Tremonti C., Kauffmann G., Heckman T., Brinkmann J., 2004, MNRAS, 351, 1151

Brinks E., 2006, The Definitive Guide to Calculating HI Masses

Broeils A. H., Rhee M.-H., 1997, A&A, 324, 877

Calzetti D., et al., 2018, ApJ, 852, 106

Catinella B., et al., 2010, MNRAS, 403, 683

Cluver M. E., Jarrett T. H., Kraan-Korteweg R. C., Koribalski B. S., Appleton P. N., Melbourne J., Emonts B., Woudt P. A., 2010, ApJ, 725, 1550

Cluver M. E., et al., 2014, ApJ, 782, 90

Cluver M. E., Jarrett T. H., Dale D. A., Smith J.-D. T., August T., Brown M. J. I., 2017, ApJ, 850, 68

Cluver M. E., et al., 2020, arXiv e-prints, p. arXiv:2006.07535

Daddi E., et al., 2007, ApJ, 670, 156

Davé R., Rafieferantsoa M. H., Thompson R. J., Hopkins P. F., 2017, MNRAS, 467, 115

Dessauges-Zavadsky M., Verdugo C., Combes F., Pfenniger D., 2014, A&A, 566, A147

Elmegreen B. G., Hunter D. A., 2015, ApJ, 805, 145

Elson E. C., Kam S. Z., Chemin L., Carignan C., Jarrett T. H., 2019, MNRAS, 483, 931

Evans II N. J., Heiderman A., Vutisalchavakul N., 2014, ApJ, 782, 114

Fumagalli M., Gavazzi G., 2008, A&A, 490, 571

Grootes M. W., et al., 2013, ApJ, 766, 59

Guo K., Zheng X. Z., Wang T., Fu H., 2015, ApJ, 808, L49

Henriques B. M. B., White S. D. M., Thomas P. A., Angulo R., Guo Q., Lemson G., Springel V., Overzier R., 2015, MNRAS, 451, 2663

Huang S., Haynes M. P., Giovanelli R., Brinchmann J., 2012, ApJ, 756, 113

Huchra J., et al., 2005, in Fairall A. P., Woudt P. A., eds, Astronomical Society of the Pacific Conference Series Vol. 329, Nearby Large-Scale Structures and the Zone of Avoidance. p. Fairall

Ilbert O., et al., 2015, A&A, 579, A2

Jarrett T. H., Chester T., Cutri R., Schneider S., Skrutskie M., Huchra J. P., 2000, AJ, 119, 2498

Jarrett T. H., et al., 2013, AJ, 145, 6

Jarrett T. H., et al., 2017, ApJ, 836, 182

Jarrett T. H., Cluver M. E., Brown M. J. I., Dale D. A., Tsai C. W., Masci F., 2019, arXiv e-prints, p. arXiv:1910.11793

Kamphuis J. J., Sijbring D., van Albada T. S., 1996, A&AS, 116, 15

Karachentsev I. D., Karachentseva V. E., Huchtmeier W. K., Makarov D. I., 2004, AJ, 127, 2031

Kennicutt Jr. R. C., 1989, ApJ, 344, 685

Kennicutt Jr. R. C., 1998, ApJ, 498, 541

Kereš D., Katz N., Weinberg D. H., Davé R., 2005, MNRAS, 363, 2

Kettlety T., et al., 2018, MNRAS, 473, 776

Kim J.-h., Krumholz M. R., Wise J. H., Turk M. J., Goldbaum N. J., Abel T., 2013, ApJ, 779, 8

Koribalski B. S., et al., 2018, MNRAS, 478, 1611

Krumholz M. R., Dekel A., McKee C. F., 2012, ApJ, 745, 69

Leitner S. N., 2012, ApJ, 745, 149

Leroy A. K., Walter F., Brinks E., Bigiel F., de Blok W. J. G., Madore B., Thornley M. D., 2008, AJ, 136, 2782

Leroy A. K., et al., 2013, AJ, 146, 19

Lia C., Portinari L., Carraro G., 2002, MNRAS, 330, 821

Liu G., Koda J., Calzetti D., Fukuhara M., Momose R., 2011, ApJ, 735, 63

Maddox N., Hess K. M., Obreschkow D., Jarvis M. J., Blyth S.-L., 2015, MNRAS, 447, 1610

Maddox N., Jarvis M. J., Oosterloo T. A., 2016, MNRAS, 460, 3419

Martinsson T. P. K., 2011, PhD thesis, University of Groningen

Meidt S. E., et al., 2012, ApJ, 744, 17

Meidt S. E., et al., 2014, ApJ, 788, 144

Michałowski M. J., et al., 2015, A&A, 582, A78

Mould J. R., et al., 2000, ApJ, 529, 786

Namumba B., Carignan C., Foster T., Deg N., 2019, MNRAS, 490, 3365

Noeske K. G., et al., 2007, ApJ, 660, L47

Noordermeer E., van der Hulst J. M., Sancisi R., Swaters R. A., van Albada T. S., 2005, A&A, 442, 137

Oh S.-H., de Blok W. J. G., Walter F., Brinks E., Kennicutt Jr. R. C., 2008, AJ, 136, 2761

Onodera S., et al., 2010, ApJ, 722, L127

Oosterloo T., Fraternali F., Sancisi R., 2007, AJ, 134, 1019

Parkash V., Brown M. J. I., Jarrett T. H., Bonne N. J., 2018, ApJ, 864, 40

Peng Y.-j., et al., 2010, ApJ, 721, 193

Ponomareva A. A., Verheijen M. A. W., Bosma A., 2016, MNRAS, 463, 4052

Ponomareva A. A., Verheijen M. A. W., Papastergis E., Bosma A., Peletier R. F., 2018, MNRAS, 474, 4366

Querejeta M., et al., 2015, ApJS, 219, 5

Roberts M. S., 1969, AJ, 74, 859

Robotham A. S. G., Obreschkow D., 2015, Publ. Astron. Soc. Australia, 32, e033

Rodighiero G., et al., 2010, A&A, 518, L25

Rownd B. K., Young J. S., 1999, AJ, 118, 670

Sancisi R., Fraternali F., Oosterloo T., van der Hulst T., 2008, A&ARv, 15, 189

Schmidt M., 1959, ApJ, 129, 243

Schruba A., et al., 2011, AJ, 142, 37

Sheth K., Vogel S. N., Regan M. W., Teuben P. J., Harris A. I., Thornley M. D., 2002, AJ, 124, 2581

Sparre M., et al., 2015, MNRAS, 447, 3548

Speagle J. S., Steinhardt C. L., Capak P. L., Silverman J. D., 2014, ApJS, 214, 15

Stevens A. R. H., Diemer B., Lagos C. d. P., Nelson D., Obreschkow D., Wang J., Marinacci F., 2019, MNRAS, 490, 96

Swaters R. A., 1999, PhD thesis, , Rijksuniversiteit Groningen, (1999)

Swaters R. A., van Albada T. S., van der Hulst J. M., Sancisi R., 2002, A&A, 390, 829

Tully R. B., Rizzi L., Shaya E. J., Courtois H. M., Makarov D. I., Jacobs B. A., 2009, AJ, 138, 323

Tully R. B., et al., 2013, AJ, 146, 86

Verheijen M. A. W., Sancisi R., 2001, A&A, 370, 765

Wang J., et al., 2013, MNRAS, 433, 270

Wang J., et al., 2014, MNRAS, 441, 2159

Wang J., Koribalski B. S., Serra P., van der Hulst T., Roychowdhury S., Kamphuis P., Chengalur J. N., 2016, MNRAS, 460, 2143

Wang J., Catinella B., Saintonge A., Pan Z., Serra P., Shao L., 2020, ApJ, 890, 63

Wilcots E. M., Miller B. W., 1998, AJ, 116, 2363

Wong T., Blitz L., 2002, ApJ, 569, 157

Wuyts S., et al., 2011, ApJ, 742, 96

de Blok E., Fraternali F., Heald G., Adams B., Bosma A., Koribalski B., 2015, Advancing Astrophysics with the Square Kilometre Array (AASKA14), p. 129

de Vaucouleurs G., de Vaucouleurs A., Corwin Jr. H. G., Buta R. J., Paturel G., Fouqué P., 1991, Third Reference Catalogue of Bright Galaxies. Volume I: Explanations and references. Volume II: Data for galaxies between 0^h and 12^h. Volume III: Data for galaxies between 12^h and 24^h.

van der Hulst J. M., van Albada T. S., Sancisi R., 2001, in Hibbard J. E., Rupen M., van Gorkom J. H., eds, Astronomical Society of the Pacific Conference Series Vol. 240, Gas and Galaxy Evolution. p. 451

APPENDIX A: SAMPLE SELECTION BASED ON INFRARED PHOTOMETRY

When choosing our sample from the WHISP survey, we considered the photometry in the corresponding WISE 3.4 μm (W1) images. Galaxies with bright foreground stars whose flux dominated the W1 flux as well as galaxies with interacting stellar disks were rejected. Figure A1 shows examples of accepted and rejected cases.

APPENDIX B: ADOPTED DISTANCES

The distances used in this study were obtained from two sources: the Cosmic Flows catalog (CF2) (Tully et al. 2013) via the Extragalactic Distance Database (EDD)[7] (Tully et al. 2009) and the NASA/IPAC Extragalactic Database (NED)[8]. The NED distances are estimates from redshift-derived radial velocities (V = cz) corrected for peculiar flows due to the influence of the Virgo cluster, the Great Attractor and the Shapley supercluster (Mould et al. 2000). The EDD distances are based on different surveys, namely, The 2Micron All Sky Survey Extended Source Catalog (2MASX, Jarrett et al. 2000), The Catalog of Neigbouring Galaxies (Karachentsev et al. 2004), and the 2MASS V8k catalog (Huchra et al. 2005), as well as independent distance derivations from archival data by Tully et al. (2009).These sources had varying methods of deriving their distances, and hence the EDD distances are

weighted averages of several methods; the Cepheid period-luminosity relation (C), Tip of the Red Giant Branch method (TRGB), Supernovae type 1a (SNIa), Tully-Fisher relation (TFR) method and the Fundamental plane (FP) method. The Cepheids method and FP method get the highest and lowest weights respectively. When obtaining distances from the EDD, we took only distances with estimates from the first four methods. The EDD database assigns a 20% uncertainty to the distance estimates. For galaxies that were not listed on EDD or had only FP-based estimates, distances were obtained from the NED Mould flow estimates. Since the distance estimates given in the EDD are scaled by a value of $H_0=74.4 \pm 3.0$ km s^{-1}Mpc^{-1}, the Mould flow parameters were also set to match the same cosmological parameters ($H_0=74.4 \pm 5.0$ km s^{-1}Mpc^{-1}, with $\Omega_m=0.27$ and $\Omega_\Lambda=0.73$). Table E2 lists the adopted distances and their associated uncertainties. The distance uncertainties were taken as the dominant contributor of uncertainty in the M_{HI} error budget.

APPENDIX C: NON-DETECTIONS FOR THE SFMS RELATION

The most dominant flux source in the WISE 11.6 μm band is continuum from warm dust grains which are more prevalent in the ISM of star forming spirals than in dwarf galaxies and dust-free ellipticals (Cluver et al. 2017). As a result, 48 galaxies (mostly dwarfs) in our original sample were below the detection threshold of the W3 band. In Sections 4.3 and 4.4, we used a sub-sample of galaxies from our main sample which had detections in the 11.6 μm band. The undetected galaxies were mostly low mass dwarfs and dust free spheroids. Figure C1 below is a histogram of the stellar masses of the undetected galaxies, while Figure C2 is an example galaxy detected in W1 but not in W3.

---

[7] http://edd.ifa.hawaii.edu/
[8] https://ned.ipac.caltech.edu/
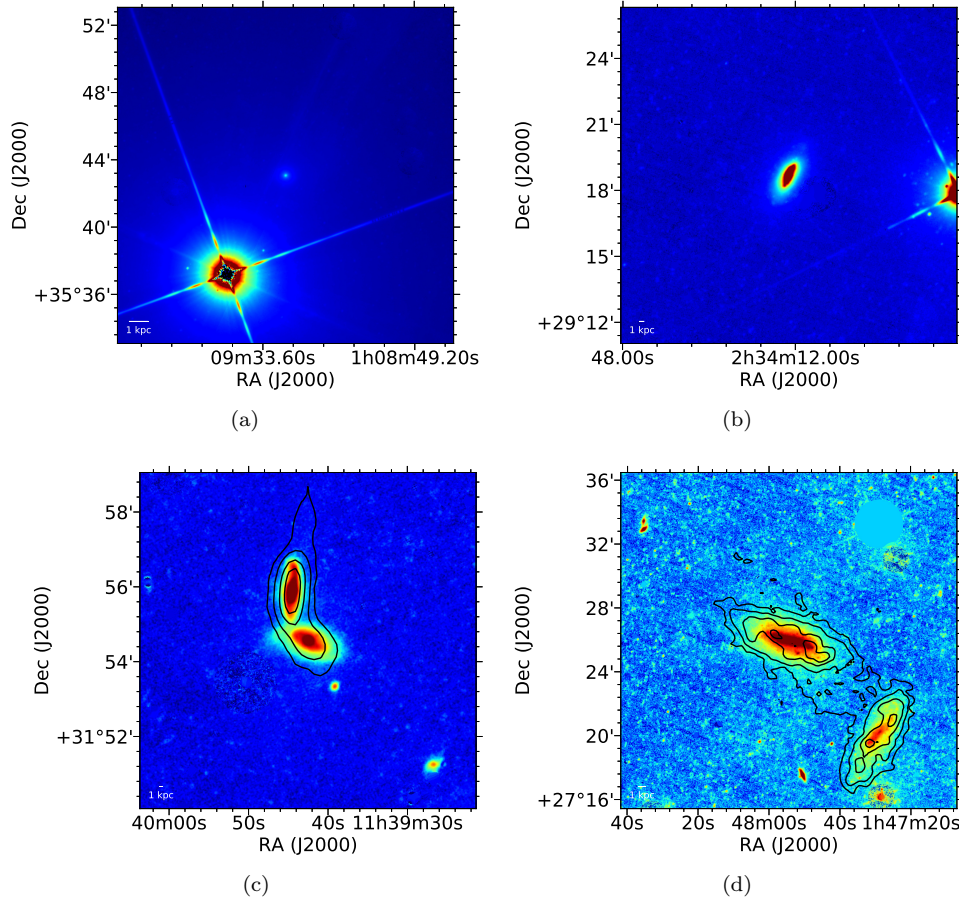
(a)

(b)

(c)

(d)

Figure A1. Top panels - WISE W1 images with foreground stars; Galaxies where the image flux was dominated by a foreground star (a) were dropped from the sample, unlike images where a bright foreground star did not dominate the flux (b). Bottom panels - W1 images of interacting galaxies. Black contours trace the HI distribution at levels of 0.032 Jy km s^{-1}, 0.081 Jy km s^{-1} , 0.16 Jy km s^{-1} and 0.24 Jy km s^{-1}; Wherever the interaction was close enough to be picked up in the infrared, such targets were dropped from the sample. Panel (c) shows one such example (UGC6621/UGC6623), while panel (d) shows a case where the infrared stellar disks are well separated (UGC1256/UGC1249).
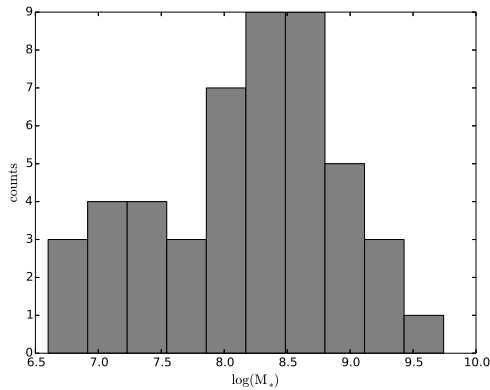
Figure C1. A histogram of galaxies in the main sample that were not detected in W3 and are thus not included in the analysis of star formation properties. These galaxies also did not have detections in the W4 band. The majority of them are dwarf galaxies and relatively dust-free, with very low MIR emission that lies below the detection threshold.
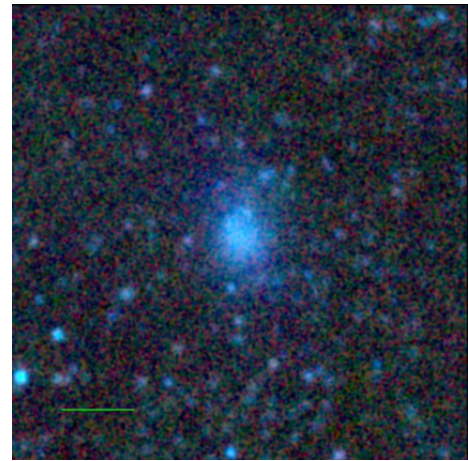
Figure C2. From our original sample of 228 galaxies, 48 (mostly dwarf) galaxies, were undetected in W3. Shown here is a WISE three-color (3.4 μm, 4.6 μm and 12 μm) image of UGC7125, a late type dwarf galaxy. The green scale bar in the lower left shows an angular scale of 1 arcmin (1.5 kpc).

APPENDIX D: GLOBAL PROFILE LINE WIDTHS

Global profiles were obtained using the MIRIAD *mbspect* task. The data points in the profiles were interpolated, and the 50% and 20% levels of the peak flux were located on either side of the global profile. The separation between the two velocities on either side of the profile at 50% peak flux level was recorded as the W_{50} linewidth, and likewise for the W_{20} linewidth. The linewidths were corrected for instrumental broadening using the method of Verheijen & Sancisi (2001);

$$
\begin{aligned}
W'_{20} &= W_{20} - 35.8 \left[\sqrt{1 + \left(\tfrac{R}{23.5}\right)^2} - 1 \right] \\
W'_{50} &= W_{50} - 23.5 \left[\sqrt{1 + \left(\tfrac{R}{23.5}\right)^2} - 1 \right],
\end{aligned}
\tag{D1}
$$

where R is the instrumental resolution in units of km/s, W_{20} and W_{50} are the observed linewidths, W'_{20} and W'_{50} are the corrected linewidths.

APPENDIX E: TABLES

Tables E1, E2, E3 and E4 show the HI observational parameters, the derived HI global properties, WISE photometric parameters and derived global infrared properties of the sample respectively.

This paper has been typeset from a TEX/LATEX file prepared by the author.

Table E1. Observational parameters of HI data from the WHISP survey.

Note: Col (2-3) - RA(J2000) and Dec(J2000), Cols (4-6) - Beam resolution (major and minor axis) and position angle. This study makes use of the WHISP data at resolution 30" x 30". Col (7) - Average noise in cubes before primary beam correction. Col (8) - Number of velocity channels, dependent on the WHISP flux density category($< 100\text{mJy}, 100\text{mJy} - 300\text{mJy}, > 300\text{mJy}$). Col (9) - Velocity resolution of the cube. (*This table is available in it's entirety in the online journal.*)

Name	R.A.	Dec	B_{maj}	B_{min}	BPA	Noise	Channels	ΔV
	deg	deg	$''$	$''$	deg	mJy beam^{-1}		km s^{-1}
(1)	(2)	(3)	(4)	(5)	(6)	(7)	(8)	(9)
UGC89	2.4725	25.9238	35.91	23.91	0	0.72	127	8.4
UGC192	5.0723	59.3038	30.81	30.48	90	7.14	127	2.1
UGC232	6.1612	33.2562	40.66	30.93	0	0.88	127	8.4
UGC485	11.7845	30.3409	28.48	24.01	0	1.75	63	16.8
UGC528	13.018	47.5505	30.0	30.0	0	4.26	127	4.1
UGC624	15.1517	30.669	43.84	32.93	0	0.63	127	8.4
UGC625	15.2309	47.682	28.33	28.32	0	1.96	63	16.6
UGC655	16.0052	41.8429	31.87	26.08	0	4.15	127	4.1
UGC690	16.8865	39.4001	29.98	25.17	0	1.79	63	16.8
UGC731	17.6833	49.6022	30.0	30.0	0	4.3	127	4.1

Table E2. HI global properties.

Note: Col (2) - Systemic velocity. Col (3-4) - Global profile linewidths at the 20% and 50% levels. Col (5) - HI radius measured at Σ_{HI} = 1M$_\odot$pc^{-2}. Col (6-7) - Integrated HI flux and total HI mass. Col (8) - Relative log uncertainty on mass. Col (9-10) - Distance in Mpc and associated uncertainty. Col (11) - The literature source of the distances, with NED for Mould flow model estimates from the NED database and CF2 for Cosmic flow database. (*This table is available in it's entirety in the online journal.*)

Name	V_{sys}	W_{20}	W_{50}	R_{HI}	$\int$Sdv	M_{HI}	$e(M_{HI})$	D	e(D)	Ref
	km s^{-1}	km s^{-1}	km s^{-1}	$''$	Jy km s^{-1}	log(M$_\odot$)	Mpc	Mpc	Mpc	
(1)	(2)	(3)	(4)	(5)	(6)	(7)	(8)	(9)	(10)	(11)
UGC89	4509.8	425.2	371.9	82	6.8	9.66	0.17	53.7	10.7	CF2
UGC192	−366.4	69.7	52.1	403	241.0	7.49	0.05	0.7	0.0	CF2
UGC232	4779.1	272.8	252.4	100	8.3	9.91	0.06	64.2	4.5	NED
UGC485	5167.4	370.0	349.5	105	14.8	10.22	0.06	69.2	4.8	NED
UGC528	661.7	129.2	82.2	100	13.7	8.6	0.06	11.1	0.8	NED
UGC624	4709.6	543.4	509.1	121	21.8	10.5	0.17	78.3	15.7	CF2
UGC625	2630.7	348.0	328.6	174	37.3	9.93	0.17	31.2	6.2	CF2
UGC655	801.3	127.3	115.5	155	20.1	8.92	0.06	13.2	0.9	NED
UGC690	5788.5	315.3	297.7	69	3.6	9.71	0.06	77.6	5.4	NED
UGC731	618.7	143.4	129.6	188	44.4	9.12	0.06	11.3	0.8	NED

Table E3. Photometric parameters of Infrared data from WISE.

Note: Cols (2-3) - Axial ratio and position angle of the stellar disk, measured in the W1 band. Col (4) - Semi major axis of the 1σ isophote in W1. Cols (5-10) W1, W3 and W4 Vega magnitudes, with corresponding magnitude errors, which were used to calculate the signal to noise ratio in the respective bands. The SNR in W3 was used to find a detection threshold for the sub-sample of 180 galaxies described in Section 2. Cols (11-12) - W1-W2 and W2-W3 color indices. Col (13) - Morphologies. (*This table is available in it's entirety in the online journal.*)

Name	b/a	pa	$R1_{iso}$	mag$_1$	Δmag$_1$	mag$_3$	Δmag$_3$	mag$_4$	Δmag$_4$	W1W2	W2W3	Morph
		deg	$''$	mag	mag	mag	mag	mag	mag	mag	mag	
(1)	(2)	(3)	(4)	(5)	(6)	(7)	(8)	(9)	(10)	(11)	(12)	(13)
UGC89	0.65	169.3	100.03	8.57	0.01	4.81	0.01	2.37	0.01	0.13	3.63	Sa
UGC192	0.87	125.8	440.03	5.11	0.01	2.32	0.01	−0.32	0.01	0.08	2.71	Im
UGC232	0.62	10.3	58.55	10.48	0.01	7.08	0.01	4.34	0.01	0.1	3.34	Sa
UGC485	0.23	179.3	84.1	10.51	0.01	7.57	0.02	6.16	0.06	0.07	2.88	Scd
UGC528	0.97	173.2	122.95	7.44	0.01	3.42	0.01	1.41	0.01	0.18	3.84	Sb
UGC624	0.52	109.2	109.12	8.94	0.01	5.43	0.01	3.78	0.01	0.1	3.44	Sab
UGC625	0.33	152.3	134.55	9.11	0.01	5.5	0.01	3.75	0.02	0.12	3.48	Sbc
UGC655	0.82	130.4	58.62	11.46	0.01	10.99	0.09	10.12	0.78	0.01	0.57	Sm
UGC690	0.72	93.9	69.02	10.22	0.01	7.03	0.01	5.4	0.03	0.07	3.15	Scd
UGC731	0.56	68.5	88.97	11.61	0.01	13.4	0.23	11.63	1.54	0.12	nan	Im

Table E4. Derived properties of the WISE data (Jarrett et al. 2019).

Note: Cols(2-4) - The signal to noise ratios in the W1, W3 and W4 bands. Cols (5-7) - Fluxes in the W1, W3 and W4. The W1 fluxes were not corrected for non-stellar sources of radiation, hence the derived stellar masses are to be taken as upper boundaries (see Section 3.4). Cols(8-9) - Stellar masses and associated (relative logarithmic) errors. Cols (10-13) - Star formation rates from the respective bands and corresponding errors. (*This table is available in it's entirety in the online journal.*)

Name	SNR_{W1}	SNR_{W3}	SNR_{W4}	W1 mJy	W3 mJy	W4 mJy	$\log(M_*)$ $M_\odot$	$e(M_*)$ $M_\odot$	$\log(SFR_{W3})$ $M_\odot$ yr^{-1}	$e(SFR_{W3})$ $M_\odot$ yr^{-1}	$\log(SFR_{W4})$ $M_\odot$ yr^{-1}	$e(SFR_{W4})$ $M_\odot$ yr^{-1}
(1)	(2)	(3)	(4)	(5)	(6)	(7)	(8)	(9)	(10)	(11)	(12)	(13)
UGC89	98.7	90.5	90.5	110.4	327.7	904.1	10.78	0.1	1.03	0.15	1.17	0.17
UGC192	98.7	90.5	90.5	2790.7	3110.0	10 600.7	8.6	0.1	−1.4	0.15	−1.26	0.17
UGC232	90.5	83.5	83.5	18.7	40.8	149.9	10.26	0.1	0.37	0.15	0.6	0.17
UGC485	90.5	67.8	67.8	18.4	25.9	32.5	10.41	0.1	0.25	0.15	0.05	0.17
UGC528	98.7	98.7	98.7	320.3	1202.3	2128.3	9.77	0.1	0.32	0.15	0.26	0.17
UGC624	98.7	90.5	90.5	76.6	186.6	261.9	11.05	0.1	1.1	0.15	0.97	0.17
UGC625	98.7	90.5	90.5	67.8	174.3	256.6	10.13	0.1	0.37	0.15	0.24	0.17
UGC690	90.5	77.5	77.5	23.7	41.7	58.6	10.62	0.1	0.52	0.15	0.37	0.17